ELSEVIER

Chemical Engineering Science 62 (2007) 3538–3548

Chemical Engineering Science

www.elsevier.com/locate/ces

A multiscale front tracking method for compressible free surface flows

Zhiliang Xu[a,*], James Glimm[b,c], Yongmin Zhang[b], Xinfeng Liu[b]

[a]*Department of Mathematics, University of Notre Dame, Notre Dame, IN 46556, USA*
[b]*Department of Applied Mathematics and Statistics, University at Stony Brook, Stony Brook, NY 11794-3600, USA*
[c]*Computational Science Center, Brookhaven National Laboratory, Upton, NY 11973-6000, USA*

Received 30 June 2006; received in revised form 26 February 2007; accepted 7 March 2007
Available online 23 March 2007

Abstract

We present an overview of multiscale computations for free surface flows based on the front tracking method. Our approach combines theory, numerical algorithm development, simulation-based scientific studies, and the analysis of experimental data.

Keywords: Front tracking; Phase transition; Compressible flow; Turbulent mixing

1. Introduction

The computation and modeling of hydrodynamics of free surface flows are basic tasks for many applications, including jet breakup, spray formation (Xu et al., 2006b), turbulent mixing (George et al., 2002) and combustion (Amsden et al., 1989). The modeling and computation of these fluid problems at the continuum level has achieved impressive success with the increasing capabilities of computational hardware, and new developments for algorithms and theories. Many fluid interface problems can be described at a single scale. Often, simple boundary conditions such as Rankine–Hugoniot jump condition at the fluid interfaces are sufficient to describe flow dynamics.

In this paper, we consider the opposite case, in which free surfaces require a multiscale description. This multiscale requirement arises for one or both of two basic reasons. The interface may become unstable and occupy a sizable volume, for which an averaged macroscale) description is useful. At a microscopic scale level, the resolution of processes internal to a "sharp" interface, such as resolved chemistry, thermal or diffusion layers, introduces a smaller spatial and temporal scale to the problem. These small scale/(microscale) phenomena may modify or even serve to define the interface description.

In this paper, we present examples of the coupling of interface dynamics to both macroscale and subscale phenomena. We refer to the scale of the interface itself as the intermediate scale. Multiscale ideas have a long history, and include such standard tools as the multigrid method (Brandt, 1977; Hackbusch, 1985), and adaptive mesh refinement (Berger, 1987; Berger and Colella, 1989). There are two principal approaches to the treatment for fluid problems involving free surfaces or fluid interface discontinuities. The first, the front capturing approach, represents discontinuities as steep gradients resolved over a small number of finite difference grids. The second, the front tracking approach, treats the interface as an internal free-moving boundary in the flow field.

The front tracking method also has a long history for the solution of fluid problems involving a single scale. A front tracking code FronTier has been developed by Glimm's group for many years and has been successfully used to simulate 2D and 3D problems. We refer to Bukiet (1988), Bukiet et al. (1986), Chern et al. (1986), and Glimm et al. (2003b) for detailed discussions of the front tracking method, its applications and the FronTier code. Using this method in a multiscale setting, however, is relatively new. The multiscale method proposed in the present paper goes beyond common multiscale methods including the multigrid method which use the same mathematical and physical model at different length scales. It is also different from the hybrid numerical methods that couple molecular

* Corresponding author. Tel.: +1 574 631 3423; fax: +1 574 631 6579.
E-mail address: zxu2@nd.edu (Z. Xu).

0009-2509/$ - see front matter © 2007 Elsevier Ltd. All rights reserved.
doi:10.1016/j.ces.2007.03.026

dynamics to a continuum formulation. In these hybrid methods, the more accurate and detailed molecular dynamics models are used to describe processes internal to the interface layer. For example, Hadjiconstantinous used molecular dynamics simulations to obtain the boundary conditions for computations at the continuum level (Hadjiconstantinous, 1999). A discussion of the general framework of these hybrid methods can be found in Weinan and Bjorn (2003) and Weiqing and Weinan (2005) and references there within. We believe that the issue we address, of coupling of distinct continuum scales but with different physics at each scale, has wide importance. There are also other methods developed to study multiscale problems, such as renormalization group methods (Wilson, 1975). Discussions regarding the design of multiscale methods in a generic form can be found in Glimm and Sharp (1997).

Two fluid problems: cavitating bubbly flow and chaotic mixing, which have important multiscale aspects, are discussed in this paper. These two fluid problems have similar as well as different properties. For both problems, there are complex microscopic interactions, including forces driving rapid transitions within a thin fluid layer, such as thermal or mass diffusion; reactive chemistry resolved within a flame width raises similar issues. We use a sharp interface model to describe fluid interfaces, which is defined as a front. These interactions are considered as the interior structure of the front, and thus are treated at a microscale. They are not resolved in many simulations and instead are modeled at a subgrid level, due to the larger scales that have to be resolved in these simulations. In the case of cavitating bubbly flow, a thermal diffusion layer at the interfacial phase transition is the microscopic scale. The state variables of the solutions defined on the finite difference grids as well as on the front are the intermediate scale. The statistical distribution of bubbles defines the macroscale, and is our primary interest. In the case of a chaotic mixing, because the interface expands chaotically, there is an averaged scale for which a volume (the mixing zone) is occupied by the interface. We define this scale as the macro scale, where the statistical properties of the front (the mixing zone) but not its detailed description are of central interest. The front serves as a bridge (the intermediate scale) to couple the microscale to the macroscale for both cases.

For any such multiscale problem, depending on its parameters, and on the length scale considered, all or only some of these scales are resolved, while the remainders are modeled. Similarly, the mathematical formulation and the choice of the appropriate numerical methods depend on the parameters and the solution scales as well. The two examples we present here illustrate these points. The outline proceeds as follows: for the fluid problems studied here, the model is the compressible Navier–Stokes equations. The governing equations can be put into the conservation form,

$$U_t + \nabla \cdot F = G. \tag{1.1}$$

We apply a finite difference solver at the intermediate flow scale on the finite difference grid. On the fluid interface, the microscopic physics, which are subgrid phenomena, are modeled through micro models or subgrid models. Moreover, our interest is to resolve the dynamics of the interface at the intermediate level in the case where the flow state variables are not specified by the flow scale alone. We must couple the microscale model to the intermediate scale to determine these state variables on the fluid interface. Therefore, the information needed by the finite difference solver will be extracted from the micro models. The updating of the flow state on the finite difference grid follows, and the front serves a freely moving boundary condition during the update. The modeling of the subscale phenomena is through analytic or simple numerical formulas. From the computational perspective, there are two major solver components. The first is a finite difference solver or scheme to obtain the flow state. The second is a microscopic solver for the subgrid model to provide the missing interface data. The implementation of these two solvers in the context of the front tracking method will be described in Sections 2 and 3.

A further step is to solve the macroscale through direct solutions of the averaged equations. We will describe this method for chaotic fluid mixing in Section 5. Chaotic flows display a wealth of detail which is not reproducible, neither experimentally nor in simulations. Generally speaking, this detail is not relevant, and fortunately, only the statistical averages of the detail are of importance. Thus direct numerical simulation (DNS) of mix gives more information than what is needed, information which in detail cannot be reproduced. Of course, the statistical averages of the details can also obtained from the Monte Carlo simulations. Since we really want the averages of the DNS simulations which can be obtained using a Monte Carlo technique, the natural question is to find averaged equations which will compute the averaged quantities directly, without use of the costly Monte Carlo step. The averaged equations can therefore be solved efficiently since there remains only one single scale, the macroscale. To close the system, the macroscopic interface data will be supplied either by a closure model or by direct Monte Carlo simulations at the microscopic level. On the other hand, DNSs in the micro and intermediate scales can serve as a validation tool for the macroscopic closure model.

The paper is organized as follows. Sections 2–4 are devoted to the micro to intermediate modeling method. Section 2 describes the front tracking solvers. In Section 3, two subgrid models are developed for interfacial phase transitions and mass diffusion, respectively. Section 4 presents the multiscale modeling of an unsteady cavitating flow, which integrates the two different scales described in Sections 2 and 3. Section 5 is used to describe the modeling of the chaotic mixing problem, which presents a model for obtaining macroscopic coherent structure within a turbulent mixing layer and solutions using both micro to intermediate and intermediate to macro modeling. The mixing edge dynamics can be supplied by either a closure model or averaging direct numerical simulations with physical mass diffusion. Numerical examples are presented in Section 6, including solutions of the averaged equations.

2. The numerical algorithm

The front tracking method is an adaptive method in which a lower dimensional moving grid is fit to and follows the dynamical evolution of waves or fluid interfaces in a flow. Two

separate grids to describe the solution are a rectangular finite difference grid and a lower dimensional grid that represents the location of the tracked wave fronts. The solution to the system is described by its values defined at the points of the rectangular finite difference grid and by their limit values on both sides of the tracked wave fronts. The tracking algorithm can be divided into two major components: the front propagation step and the interior state update step. The propagation of the front position and states is performed in the front propagation step. Operator splitting separates the front propagation step into direction normal to and tangent to the front two sub-steps. The update of the states on the rectangular finite difference grid follows the front propagation step. Special care is needed only when the stencil cut by a front. In this case, the missing points of the stencil are obtained by extrapolation.

In the multiscale setting, we still need these two components. However, the microphysics within the interfacial layer has to be considered. A brief description is given below.

2.1. The front propagation algorithm

The front propagation algorithm which is responsible for the propagation of points of the front is the key step for the front tracking method. We solve the hyperbolic conservation laws of the form

$$U_t + n \cdot [(n \cdot \nabla) F(U)] = G, \tag{2.1}$$

where n is the unit vector normal to the front to obtain the new front position and the updated limiting values of the flow states on two sides of the front. This is called the normal propagation step. The computation of the normal direction n in a higher dimension is discussed in Jian et al. (2006). Eq. (2.1) is obtained by operator splitting at each point on the tracked front. Depending on the microscale physics modeled, G could represent heat flux, mass diffusion, etc. When we model compressible inviscid fluids, Eq. (2.1) reduces to the Euler equations. For the Euler equations, the point propagation algorithm first solves Riemann problems associated with Eq. (2.1), i.e. the initial value problem of one spatial dimensional hyperbolic system with piecewise constant initial data separated by a single jump discontinuity. The solutions to Riemann problems predict the new front position. This is followed by a slope reconstruction to compute the flow gradients in the normal direction. Then a correction step is used to account for the flow gradients on both sides of the front, which is also a coupling between the propagation of the front and the states on the Euclidean grid.

The normal propagation step only uses flow information in the direction normal to the tracked front. The tangential component of Eq. (1.1) is solved after the normal propagation step. See Bukiet et al. (1986), Chern et al. (1986), and Glimm et al. (2003b) for the details.

2.2. Finite difference solvers for interior states

Standard high resolution shock capturing methods are used to update states on the Euclidean grid. The MUSCL method (Monotonic Upstream-centered Scheme for Conservation Laws) of Van Leer (1979), PPM (piecewise parabolic method) (Colella and Woodward, 1984), etc. are supported in *FronTier*. The coupling of the states on the tracked fronts to the interior states on the Euclidean grid uses the ghost cell (or ghost fluid) method, which is an extrapolation method. If the set of Euclidean grid points and states associated with these grid points, which is called a stencil to compute the state at a grid point is crossed by the tracked front, the stencil points separated from this grid point by the front use the states on the tracked front nearest to these stencil points. Therefore, the tracked front prevents the finite difference equation from using states on opposite sides of the tracked front, and keeps a sharp discontinuity at the front.

From the above discussion, we can clearly see that an important component in the macroscopic flow solvers is the interior free boundary condition provided by the front. We now describe how to extract boundary conditions from the microscopic interface models for different applications.

3. Microscopic interfacial dynamics

We will discuss two examples coupling microphysics (internal structure of the front) to the front propagation. The examples are the modeling of an interfacial phase transition and the modeling of mass diffusion across a tracked (sharp) interface. In both cases, the effects of the microphysics occurs in the examples considered here at a scale well below the computationally resolved scales, and so the effects are introduced via a subgrid model. For the phase transition boundary, the subgrid physics is a thermal conduction layer, and thus the two cases are closely related.

3.1. Interfacial phase transition

We now describe the modeling of an interfacial phase transition and the interface solver associated with it. In case of a phase transition, thermal gradients at the interface drive the mass transfer across the interface. The phase transition is governed by the compressible Euler equations with heat diffusion. In one spatial dimension, it is

$$\frac{\partial U}{\partial t} + \frac{\partial F(U)}{\partial x} = 0, \tag{3.1}$$

where $U = [\rho, \rho u, \rho E]^{\mathrm{T}}$, $F(U) = [\rho, \rho u^2 + P, \rho u E + uP - \kappa(\partial T/\partial x)]^{\mathrm{T}}$, ρ denotes density, u velocity, P pressure, $E = u^2/2 + \varepsilon$ is the specific total energy, ε is the specific internal energy, κ is a coefficient of thermal diffusion, and T is the temperature. Integrating the conservation equations (3.1) across the interface, we obtain the balance equations for the mass, momentum, and total energy, respectively,

$$[\rho u] = s[\rho], \tag{3.2}$$

$$[\rho u^2 + P] = s[\rho u], \tag{3.3}$$

$$[\rho u E + uP - \kappa \nabla T] = s[\rho E], \tag{3.4}$$

where s is the phase boundary speed. We also postulate that the temperature is continuous across the phase boundary. Therefore, the interfacial temperatures of the vapor and liquid are equal

$$T_l = T_v = T_s, \tag{3.5}$$

where T_s is the interface temperature. The subscripts "l" and "v" refers to liquid and vapor, respectively. Eqs. (3.2)–(3.4) can be manipulated to yield equations for the mass flux, linear momentum flux and energy balance at the phase boundary. For example, the mass flux is $m = \rho_v(u_v - s) = \rho_l(u_l - s)$. To complete the formulation we need to provide an equation for either the interface temperature T_s or the mass flux m. Phase change, at an atomic level, involves the interaction of vapor molecules with the liquid surface. From a kinetic theory point of view, the net mass flux of evaporation is

$$m = a\frac{P_{\text{sat}}(T) - P_v}{\sqrt{2\pi RT}}. \tag{3.6}$$

Here, $P_{\text{sat}}(T)$ is the equilibrium pressure at temperature T. a represents the ratio of molecules condensing into liquid over the total number hitting the phase boundary and is called the accommodation coefficient. Its value is often experimentally determined. For the detailed discussion, see Van Carey (1992) and references cited there. The derivation of Eq. (3.6) follows Alty and Mackay (1935).

3.1.1. A subgrid temperature gradient model

The phase transition problem requires a subgrid model to describe the thermal layer at the phase transition boundary. This is because that the width of the thermal layer of the liquid is proportional to $\sqrt{\kappa t/\rho c_p}$, and the time step restricted by the CFL condition is $\mathrm{d}t \approx \mathrm{d}x/c$. It requires 10^3–10^4 steps in the simulations we consider here for the liquid thermal layer to expand to a micron scale grid cell. For the finite difference scheme, if the thermal layer is thinner than a grid cell, the temperature profile takes the form

$$T \approx T_s + (T_{-1} - T_s)\,\mathrm{erf}\left(\frac{x}{\sqrt{4\alpha t}}\right), \tag{3.7}$$

where T_s is the phase boundary temperature, T_{-1} is the temperature one grid cell away from the phase boundary and $\alpha{=}\kappa t/\rho c_p$. Here the stretching of the interface is ignored for simplicity of the numerical algorithm. Thus the temperature gradient at the interface is approximated by

$$\frac{\partial T}{\partial x} \approx \frac{(T_{-1} - T_s)}{\sqrt{\pi\alpha t}}. \tag{3.8}$$

The interfacial heat flux in the form of $\kappa\Delta T/\Delta x$ should be replaced by the above approximation. When the thermal layer is wider than a grid cell, the conventional finite difference approximation of the temperature gradient at the interface gives satisfactory results.

To solve this system of equations numerically, the characteristic form of Eq. (3.1) together with the phase boundary conditions (Eqs. (3.2)–(3.6)) are solved. We have developed an iterative phase boundary propagation algorithm. It generalizes the numerical methods for finding the contact discontinuity of a Riemann problem, and introduces a subgrid model for finding the interface temperature. For a detailed discussion of this algorithm, we refer to Xu et al. (2006a).

3.2. A subgrid mass diffusion model

The conservation laws

$$\frac{\partial \rho_i}{\partial t} + \nabla\cdot\rho_i v = \nabla\cdot\rho_i v\nabla c_i, \tag{3.9}$$

$$\frac{\partial \rho v}{\partial t} + \nabla\cdot\rho v v = \rho g, \tag{3.10}$$

$$\frac{\partial \rho E}{\partial t} + \nabla\cdot\rho v E = \rho v\cdot g + \nabla\cdot\rho\sum_i \upsilon_i h_i\nabla c_i, \tag{3.11}$$

model the mixing of compressible miscible fluids with physical mass diffusion, where υ_i is the ith species diffusivity, $h_i = e_i + p_i/\rho_i$, $\rho = \sum_i \rho_i$ and $c_i = \rho_i/\rho$.

The difficulty in solving this system is to eliminate numerical diffusion across an interface between distinct fluids while allowing the correct amount of physical mass diffusion, in the limit where v is small relative to the affordable grid resolution. We introduce a new algorithm, building on the front tracking method, to add small amounts of physical mass diffusion while preserving the elimination of numerical mass diffusion across an interface. The new algorithm, developed first in 1D, is based on the following ideas. Untracked contact discontinuities give rise to a blurred or smeared out front. We preserve the tracking of a sharp front and introduce physical mass diffusion through it as a perturbation. Thus the time step is split into two parts, the first being the usual non-diffusive front tracking (Jian et al., 2006; Glimm et al., 1999a), and the second a pure physical mass diffusion step. Conceptually, the front states stored on the tracked front represent the states at $\pm\infty$ relative to the scale of the diffusion layer. After the diffusion layer has reached a width of $2\Delta x$, the first algorithm is turned off and replaced with the conventional finite difference method.

To update interior states, we use operator splitting to separate the hyperbolic from the parabolic terms. A regular stencil is one which does not meet the front. The diffusion term is solved by conventional centered finite differences. For an irregular stencil, if the front cuts a mesh cell not at the center of the stencil, we define ghost cell extrapolation of the states on the same side of the front as the center cell using the front states as in Glimm et al. (1980). In case the front cuts the central cell of the stencil, i.e. the cell that the stencil is updating, we use the new algorithm explained below. We distribute this increment of diffused mass ($\Delta M_{\pm}^n$), which is calculated from the analytical solution of the 1D convection equation, to the two closest grid cells which lie on each side of the center of the layer. In order to do this, we detect the closest grid center points on either side of the front center point X_c^{n+1}, namely x_i and x_{i+1}. We add to

these cells the mass diffused from the other side:

$$\rho_i^{n+1} = \tilde{\rho}_i^{n+1} + \frac{\Delta M_-^n}{\Delta x},$$

$$(\rho v)_i^{n+1} = (\tilde{\rho}\tilde{v})_i^{n+1} + \frac{\tilde{v}_i^n \Delta M_-^n}{\Delta x},$$

$$(\rho E)_i^{n+1} = (\tilde{\rho}\tilde{E})_i^{n+1} + \frac{\tilde{E}_i^n \Delta M_-^n}{\Delta x},$$

$$\rho_{i+1}^{n+1} = \tilde{\rho}_{i+1}^{n+1} + \frac{\Delta M_+^n}{\Delta x},$$

$$(\rho v)_{i+1}^{n+1} = (\tilde{\rho}\tilde{v})_{i+1}^{n+1} + \frac{\tilde{v}_{i+1}^n \Delta M_+^n}{\Delta x},$$

$$(\rho E)_{i+1}^{n+1} = (\tilde{\rho}\tilde{E})_{i+1}^{n+1} + \frac{\tilde{E}_{i+1}^n \Delta M_+^n}{\Delta x}. \tag{3.12}$$

For the higher dimension case, we split the front into normal and tangential directions. The subgrid algorithm is applied along the normal direction, and no diffusion is added to the tangential sweep. In this way, the subgrid algorithm in one dimension can be extended easily and efficiently to the higher dimension. See Liu et al. (2007) for a detailed discussion of the algorithm.

4. Multiscale modeling for multiphase flows

Here we study an unsteady cavitating flow. From theoretical considerations (Landau and Lifshitz, 1980), we assume cavitation results from the nucleation of a spherical bubble in the liquid when the liquid pressure drops below the vapor pressure. Thus we model mixed phase flow as made of small-scale vapor bubbles. There are three active length scales, namely the scale of the macro fluid flow, the scale of the interpenetrating mixture, i.e. cavitation bubbles, and the scale of a thermal gradient at the phase boundary interface. We resolve the two larger of these three length scales.

Our proposed method is different from a commonly employed modeling method, which is to develop a continuum model, or a single pseudo-fluid equation of state, of multiphase (bubbly) flows (Schmidt et al., 1999). For this class of methods, the key issue is to develop a proper constitutive law for the mixture (Ventikos and Tzabiras, 2000). Often the mixture is assumed to be homogeneous and barotropic. Despite its simplicity, this class of methods lacks an ability to resolve detailed physics such as drag, surface tension, phase transitions, viscous friction between two phases, and other microphysics phenomena. However, for certain applications, inclusion of these microphysics phenomena is critical in order to give a correct description of the macroscopic flow dynamics. Example of Section 6.1 is a simple case for these applications.

In contrast to continuum modeling methods, we have developed a discrete vapor bubble model (Xu et al., 2006b) for the first principles simulations of these problems. The discrete vapor bubble model describes the liquid–vapor/gas mixture as pure phase domains separated by free interfaces, i.e. vapor bubbles of finite size inserted into the liquid and separated from the liquid by interfaces. In our modeling process, we resolve the dynamics of the individual bubbles directly by the front tracking approach. The detailed physics such as drag, surface tension, phase transitions between two phases are included in our model. The dynamic states are directly computed on the flow scale. Therefore, the task that remains at the microscopic level is to simulate the dynamic creation of cavitation bubbles. To model this dynamic process, cavitation parameters such as the nuclei density for the bubble growth have to be given either experimentally or to be determined numerically. We first give a model to determine the cavitation parameters for the ideal fluids. We then describe how to modify this model for the simulation of real fluids for real applications.

For an unsteady cavitating flow, vapor bubbles are formed by liquid vaporization when the liquid pressure P fluctuates and falls below the saturation vapor pressure P_v at constant temperature. If we assume that bubble nucleation occurs completely within a liquid, which is called homogeneous nucleation, and define the maximum size of a nucleus by the radius R_c (critical radius), then at equilibrium, the critical tension $\Delta P_c = P_v - P$ is given by (Brennen, 1995; Landau and Lifshitz, 1980)

$$\Delta P_c = \frac{2\sigma}{R_c}, \tag{4.1}$$

where σ is the surface tension of the liquid. It should be noted that the likelihood that nucleation will occur depends on the kinetics of the vapor nucleus formation process. To create such a nucleus with critical radius R_c, a critical energy $E_c = 16\pi\sigma^3/3\Delta P_c^2$ (Brennen, 1995; Landau and Lifshitz, 1980) must be deposited into the liquid to break the barrier against nucleation. This critical energy E_c accounts only for surface energy and the gain in volume energy. Thus the nucleation probability Σ in a volume V during a time period t is (Balibar and Caupin, 2003):

$$\Sigma = 1 - \exp^{(-J_0 V t \exp(-E_c/(k_b T)))}, \tag{4.2}$$

where J_0 is a factor of proportionality defined as $J_0 = N(2\sigma/\pi m)^{1/2}$, k_b is the Boltzmann's constant, T is the absolute liquid temperature, N is the number density of the liquid (molecules/m^3) and m is the mass of a molecule. To describe a homogeneous cavitating flow, Eqs. (4.1) and (4.2) give relations among the initial (critical) bubble radius, the bubble population and critical tension. However, we note that the analysis above is applicable only to clean fluids. Due to fluid impurities, it is known that real fluids contain large concentrations of nucleation centers that increase the cavitation probability. Heterogeneous nucleation, which is nucleation at the interface between the liquid and another phase that it contacts, may also increase the cavitation probability. Thus accurate values of critical cavitation parameters are often experimentally measured. Since we are interested in the simulation of real fluids, we assume that (4.2) gives the functional relation between the critical pressure, volume, and the nucleation probability, while the absolute value of the critical volume at a specific value of the critical pressure has to be calibrated through the comparison of simulation results with experimental data.

For the real fluids, the value of the physical critical radius R_c is at the order of sub-microns, which is below the grid resolution

used for our simulations. Based on this consideration, in our model, the radius of the numerical critical (initial) vapor bubble, which is at the order of microns, replaces R_c. The value of the radius of the numerical initial bubble is also on the order of the mesh size in order to be resolved on the finite difference grids. We note that this approximation neglects the initial growth stage of sub-micron bubbles to a size allowed by the mesh resolution, and the effects of local reduction in pressure that accompanies the growth. A phenomenological bubble spacing parameter h which is defined as distance between two centers of the bubbles is chosen by a series of numerical experiments. By calibrating this parameter, we account for effects of initial growth of sub-micron bubbles and the resulting bubble population.

To simulate the dynamic creation of micro bubbles, a dynamic bubble creation algorithm is formulated to model this process. This bubble creation algorithm first identifies regions composed of cells which have pressure lower than the specified threshold. If such a region is bigger than the critical bubble size and has a distance to other bubbles larger than the specified bubble spacing, a vapor bubble is created at the center of this region. The initial vapor bubble states are computed using the static Clausius–Clapeyron relation with the given liquid temperature. To find the numerical solution at the phase boundary, the method described in Section 3.1 is used.

We note that this model has been validated for a simple multiphase system, a liquid containing fixed numbers of non-dissolvable gas bubbles, using experimental data on the dispersion and attenuation of sound waves and profiles of shock waves in bubbly water (Lu et al., 2005). When the experimental values for cavitation parameters are not available, the proper values for the bubble spacing and initial radius have to be chosen from numerical experiments. Very often one will find that some statistics values of the flow are not sensitive to the chosen of these values, while others are sensitive. When this is the case, one has to determine which values are the most important ones that define the macroscopic flow dynamics and calibrate the cavitation parameters based on these values.

5. Turbulent mixing and averaged equations

Turbulence is the prototype multiscale problem; here we consider an important subproblem, turbulent fluid mixing. Turbulent fluid mixing arises as a result of unstable and chaotic interface dynamics induced by gravitational forces, shock waves, or a combustion process. Turbulent mixing is important to the design of ICF devices, the modeling of diesel engines, and the modeling of supernova, as well as many other fluid mixing scenarios. In general the problem links three (types of) length scales: the interior of the interface, such as the laminar resolved flame front chemistry, the mesoscale of the mixing layer defined by the spatial extent of the convoluted interface or flame front and the macroscale of the large scale fluid flow. Distinct physics defines the flow in each regime, namely reactive chemistry and transport phenomena within the interface, drag, buoyancy, and the Euler or Navier Stokes balance laws in the mesoscale mixing zone and averaged equations to describe the evolution of flow statistics in the macro flow regime. Each of these length scales and flow regimes poses problems; their coupling into a single theory is a significant multiscale challenge to modern science.

5.1. Stochastic mixing models

The purpose of a turbulent mix model is to give a reduced (statistical) description of chaotic mixing. The models governing the evolution of the fluid mixing are obtained by applying an appropriate averaging procedure to microphysical equations. There are mainly two types of mixing models. Two-pressure two-phase flow models are proposed by Stewart and Wendroff (1984), Ransom and Hicks (1984), Glimm et al. (1998a), and Abgrall and Saurel (2003). They employ distinct phase pressures and lead to hyperbolic models, eliminating mathematical difficulties of complex characteristics associated with single pressure multiple velocity flow models. Single pressure dual velocity models (Drew, 1983; Wallis, 1969; Keyfitz, 1991) require mass diffusion and viscosity for their stability. After a turbulent transition, these transport parameters should be large enough to assure stability. A promising single pressure dual velocity model, (Scannapieco and Cheng, 2002), is stable even in the absence of viscous terms. An open issue is the comparison and assessment of these various models, in relation to direct simulation mixing data.

We have obtained a general model (Glimm et al., 1998a, 2003a; Jin et al., 2006) for a turbulent mixing layer. We found closed form solutions for a 1D incompressible model and for the weakly compressible asymptotics. Properties of this model suggest a coupling of the edge motions (bubble and spike edges) of a mixing zone, derived from a property of positivity of entropy of mixing. Numerical simulations based on this model were validated against the closed form solution and asymptotics we derived. Here we give a brief summary of this macroscale model for two pressure two phase flow.

The averaging process used to define the model equations can be thought of as a local spatial or temporal average, or as an ensemble average, with respect to an ensemble of random initial conditions. Several realizations lead to the consideration of a mixed zone of fluids where, on average, one finds fluid k at a given point p only a fraction $\beta_k = \beta_k(t, p)$ of the ensemble total. Clearly, $\beta_k = 1$ corresponds to a pure fluid region, where there is no mixture at all, a situation that happens away from the interface of all realizations of the ensemble. Evidently, $\beta_1 + \beta_2 = 1$.

We parametrize the fluids by the discrete index k, $k = 1, 2$, and let β_k, ρ_k, $\vec{v}_k$, p_k and E_k be the volume fraction, density, velocity, pressure and total energy of fluid k, respectively. The model we study is defined by the system of equations:

$$\partial_t \beta_k + \vec{v}^* \cdot \nabla \beta_k = 0,$$

$$\partial_t (\beta_k \rho_k) + \nabla (\beta_k \rho_k \vec{v}_k) = 0,$$

$$\partial_t (\beta_k \rho_k \vec{v}_k) + \nabla (\beta_k \rho_k \vec{v}_k \otimes \vec{v}_k) = -\nabla (\beta_k \rho_k) + p^* \nabla \beta_k + \beta_k \rho_k \vec{g},$$

$$\partial_t(\beta_k\rho_k E_k) + \nabla(\beta_k\rho_k E_k\vec{v}_k) = -\nabla(\beta_k p_k\vec{v}_k) + (p\vec{v})^*\cdot\nabla\beta_k + \beta_k\rho_k\vec{v}_k\cdot\vec{g} \quad (5.1)$$

proposed in Chen et al. (1996), Glimm et al. (1997, 1998a, 1999b), Cheng et al. (1999), and Jin et al. (2006). Here, $\vec{g}$ is the gravity and $\vec{v}^*$, p^* and $(p\vec{v})^*$ represent averages to be modeled by a closure expression,

$$\vec{v}_k^* = \mu_1^v\vec{v}_2 + \mu_2^v\vec{v}_1, \quad (5.2)$$

$$p^* = \mu_1^p p_2 + \mu_2^p p_1, \quad (5.3)$$

$$(p\vec{v})^* = p^*(\mu_1^E\vec{v}_2 + \mu_2^E\vec{v}_1) + \vec{v}(\mu_1^E p_2 + \mu_2^E p_1) - (\mu_1^E p_2\vec{v}_2 + \mu_2^E p_1\vec{v}_1), \quad (5.4)$$

The coefficients μ_k^v, μ_k^p and μ_k^E can be proved quite generally to define convex sums, so that $\mu_1^q + \mu_2^q = 1$, $\mu_k^q \geqslant 0$, $q = v, p, E$ (Glimm et al., 1998b).

The convex coefficients μ_k^q depend only on the volume fraction in a fractional linear manner, and two of the three coefficients in the fractional linear expression can be fixed from boundary conditions at the edges of the mixing zone. The remaining coefficient for $q = v$ is interpreted as the ratio of logarithmic rates of mixing volume creation; in the other two cases for q the ratio is accelerating forces and heat added for the two fluids.

5.2. Mixing edge evolution algorithm

We regard the edge positions $Z_k(t)$as input, or data, which complete the specification of the model, or close it. We appeal to the buoyancy-drag model (see Glimm et al., 1999b and references therein) to provide the $Z_k(t)$. In this sense we decouple the complete multiphase model into separate edge and interior models, with the edge model completing the closure of the entire model. With the mixing zone edge accelerations given and constitutive laws, the model has no adjustable parameters.

The mixing zone edge information will be supplied through averaging a series of direct numerical simulations with random initial data in Monte Carlo sense or a phenomenological buoyancy-drag ODE to specify the edge accelerations,

$$(-1)^k\frac{\mathrm{d}^2 Z_k(t)}{\mathrm{d}t^2} = Ag - \frac{\rho_{k'}}{\rho_k + \rho_{k'}}C_k\frac{V_k^2}{|Z_k|}, \quad (5.5)$$

where $\rho_k(V_k)$ is the density (edge velocity) of fluid k, ($k = 1, 2$, $k' = 3-k$), the Atwood number $A = (\rho_2 - \rho_1)/(\rho_2 + \rho_1)$, and C_k is the drag coefficient. Equations of the general form (5.5) are known as buoyancy-drag equations, and have been considered by a number of authors (Hansom et al., 1990; Alon et al., 1994; Cheng et al., 2000; Dimonte, 2000; Oron et al., 2001).

Here we describe the edge evolution algorithm in context of the buoyancy-drag model.

Let Z_1^n be the bubble (vanishing light fluid) mixing zone edge position, Z_2^n be the spike (vanishing heavy fluid) mixing zone edge position, $(v_1^N)_{01}^n$, $(v_2^N)_{02}^n$ be the normal velocities of fluids 1 and 2 at the corresponding positions Z_1^n and Z_2^n at time t^n. The edge position Z_k^{n+1} at the next time level t_{n+1} is updated using $Z_k^{n+1} = Z_k^n + (v_k^N)_{0k}^n\vec{N}_k\Delta t$, $k = 1, 2$ where $\vec{N}_1$ and $\vec{N}_2$ are normal vectors at Z_1^n and Z_2^n, respectively.

The heavy fluid is continuous across the bubble edge and the light fluid is continuous across the spike edge. The continuous phase states on the front are updated by interpolation from interior states after the interior update. Here we describe the update of the vanishing phase on the front by applying the method of characteristics and the buoyancy-drag law.

There is one missing characteristic at each mixing zone boundary. The resulting missing information is supplied from the buoyancy-drag equation for the mixing zone edge. We update the normal component of the vanishing phase velocity $(v_k^N)_{0k}$ on the edge k by finite differencing the buoyancy-drag equation (5.5) and noting that $(v_k^N)_{0k}$ is the same as the edge normal velocity $\dot{Z}_k(t) = V_k(t)$:

$$(v_k^N)_{0k}^{n+1} = (v_k^N)_{0k}^n + (-1)^k\Delta t \times\left\{A_{0k}^n g - C_k^d\left[\frac{(\rho_k')_{0k}^n}{(\rho_2)_{0k}^n + (\rho_1)_{0k}^n}\right]\frac{(v_k^N)_{0k}^n(v_k^N)_{0k}^n}{(Z_k)^n}\right\},$$

where A_{0k}^n is the instantaneous Atwood ratio at edge k, $A_{0k}^n = ((\rho_2)_{0k}^n - (\rho_1)_{0k}^n)/(\rho_2)_{0k}^n + (\rho_1)_{0k}^n)$.

5.3. Rayleigh–Taylor mixing rate

Fluid mixing induced by Rayleigh–Taylor (RT) instability is an important type of chaotic fluid mixing to which the above statistical mixing model can apply. RT instability occurs at a fluid interface whenever the density gradient is opposed to the acceleration gradient across the interface. The drag coefficient C_k in buoyancy-drag equation (5.5) will be fitted to the RT mixing rate. The RT mixing rate is the dimensionless coefficient α in the equation:

$$h = \alpha Agt^2 \quad (5.6)$$

for the height h of the bubbles, i.e. the interpenetration distance h of the light fluid into the heavy fluid. Here $A = (\rho_h - \rho_l)/(\rho_h + \rho_l)$ is the Atwood number and t is the time. Acceptable experimental values for α are $\alpha = 0.06 \pm 0.01$ (Smeeton and Youngs, 1987; Banerjee and Andrews, 2006). See Sharp (1984) for background information. To remove effects of mass diffusion (physical and/or numerical), we follow George and Glimm (2005) to define a time dependent Atwood number $A(t)$, and the renormalized growth rate α_{ren},

$$\alpha_{\mathrm{ren}} = \frac{h}{2\int_0^t\int_0^S A(r)g\,\mathrm{d}r\,\mathrm{d}s}.$$

Our 3D validation results are summarized in Table 1. See also Fig. 1. Here the simulations that employed TVD (total variation diminishing) method are used for the comparison and are referred as TVD simulations in Table 1 and Fig. 1. The word "ideal" refers to no physical diffusion. Please refer to Liu et al. (2006) for the details regarding these simulations. These 3D direct numerical simulations in micro and intermediate scales can be further used for the validation of statistical models for macroscale mixing.

Table 1
Mixing rates compared for an air-helium 3D Rayleigh–Taylor experiment and related simulations

Experiment simulation	Comment	α
Andrews	Miscible (Banerjee and Andrews, 2006)	0.07
FronTier	Miscible	0.069
TVD	Untracked (George and Glimm, 2005), ideal	0.035
FronTier	Ideal	0.09
TVD	Untracked, ideal (renormalized)	0.076
FronTier	Miscible, ideal (renormalized)	0.089

The simulations compare physical mass diffusion to ideal physics (no diffusion) and they compare tracked to untracked algorithms. The agreement of the tracked simulation with physical mass diffusion with the experiment is excellent, while the ideal simulations do not agree with experiment, nor (because of the numerical mass diffusion in the untracked ideal simulation) with each other.

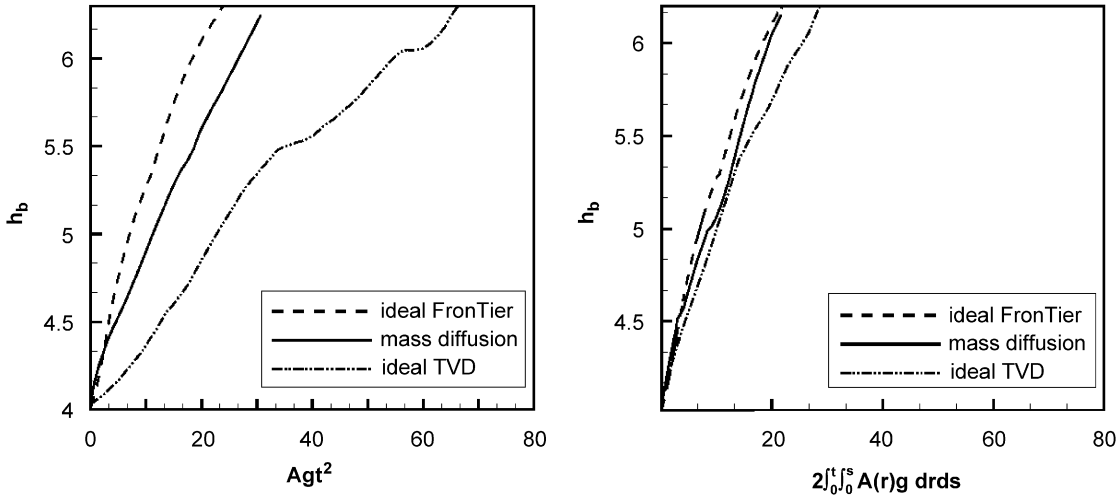

Fig. 1. Left: self-similar growth of the mixing zone. Right: the same data plotted using a time dependent Atwood number, to remove the effects of numerical or physical mass diffusion.

6. Numerical examples

In this section, we present different numerical examples to demonstrate the importance of considering flow dynamics in a multiscale manner.

6.1. Phase transition coupled with acoustic waves

In this test problem, we show that when acoustic waves and thermal diffusion are both present, the evolution of the phase boundary is determined by the coupled hydro and thermal dynamics, and therefore must be considered in a multiscale manner. We simulate the condensation of water vapor in the presence of an acoustic wave. The computation domain is from −1 to 1 cm, which is discretized into 2000 grid cells. The phase boundary is initially set at the origin with vapor on the left side and water on the right side. Both phases start at rest and have common temperature 293 K. The initial vapor pressure is 93 mbar, whose saturation temperature is 343 K. The water pressure is 193 mbar. A reflection boundary condition is used on both ends of the domain.

When the water vapor interface was treated as a pure contact discontinuity, the water first expands due to its higher pressure, then shrinks and expands periodically as the pressure wave propagates back and forth in the liquid. When the water vapor interface was treated as a phase boundary, the liquid volume still

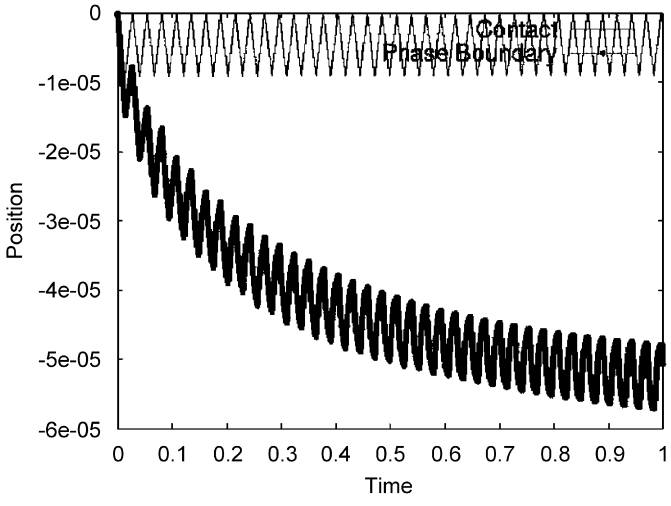

Fig. 2. The evolution of the interface separating water and water vapor. The double width solid line is for the phase boundary. The solid line is for the contact discontinuity.

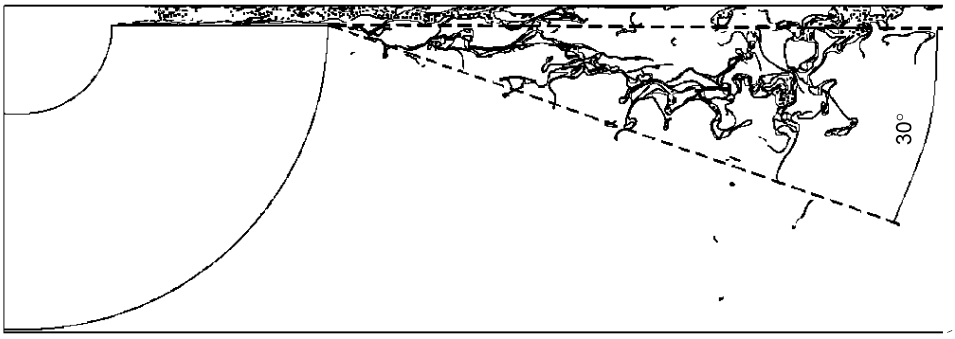

Fig. 3. Plot of jet interface at late time.

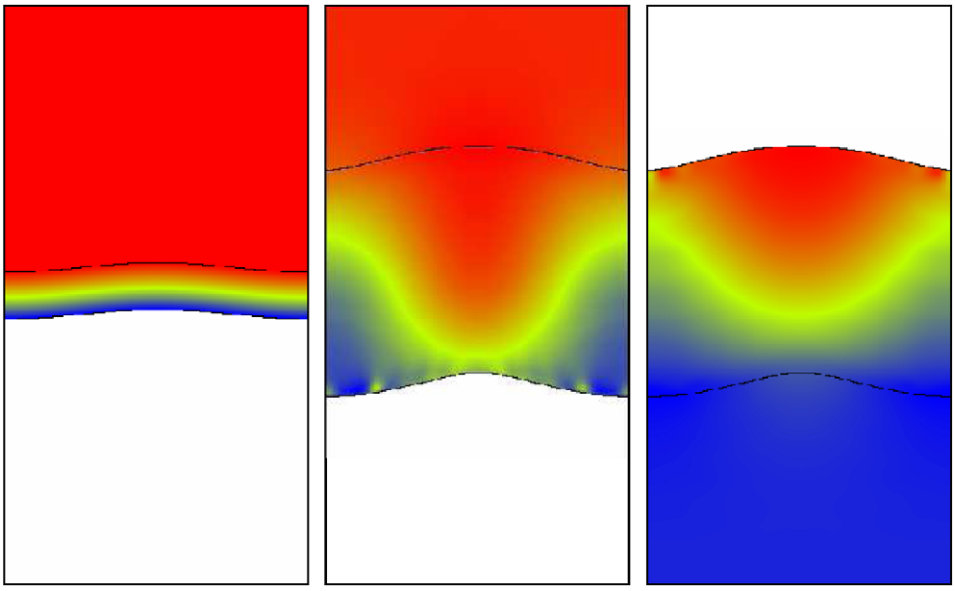

Fig. 4. The fluid velocities of the two-dimensional simulations. Left frame: light (upper) fluid velocity v_{1y} at $t = 0$. Center frame: light (upper) fluid velocity v_{1y} at $t = 3.0$. Right frame: heavy (lower) fluid velocity v_{2y} at $t = 3.0$.

oscillates, but the oscillation was superposed upon an expansion due to condensation as the vapor was over-saturated.

Fig. 2 compares the evolution of a water vapor interface with and without phase transitions. The double width solid line represents the phase boundary. The single width solid line represents the contact discontinuity. It is clear from Fig. 2 that phase transitions play an important role in the interface dynamics.

6.2. *Unsteady cavitating flow and jet atomization*

Simulations of liquid cavitation and jet atomization, i.e. jet breakup and spray formation arising from high speed nozzle flows are presented here. We simulate a flow through a nozzle with a diameter 0.178 mm and a length 1 mm. In 0.3 ms, the pressure of injected fuel rises linearly from 1 to 500 bar. Cavitation bubbles are formed due to the sharp inlet corner of the nozzle and a "vena contracta", i.e. the flow "sticks" to the edges of the opening, thus effectively reducing the size of the opening, inside the nozzle (Bergwerk, 1959). For the literature review of jet atomization mechanisms, see Reitz and Bracco (1982, 1986) and Liu and Reitz (1998).

From a computational point of view, we argue that cavitation and spray formation should be treated as multiscale phenomena. Macroscopic flow parameters, such as the spray opening angle and the volume fractions of liquid within the spray are on the scale of centimeter. The finite vapor bubble size, which is essential for the spray formation in our simulations, is on the scale of microns. The dynamics of the moving phase boundary, with mass transfer across the phase boundary, depends on a thermal diffusion layer, having width of the order of nanometers.

We used the model described in Section 4 to resolve the dynamics of cavitation bubbles in the simulations of atomization of a high speed jet within a 2D symmetric geometry. The details of the description of the problem and the numerical methods are presented in Xu et al. (2006b). We only report some of the important results here. A plot of the jet interface at late time is shown in Fig. 3. This flow is strongly compressible and vapor bubbles are created constantly. Thus capabilities developed

here are required to carry out the simulation. From the simulation of flow in the nozzle, the void fraction which is defined as the ratio of the vapor volume to the volume of the nozzle is not sensitive to the choice of the critical bubble radius. On the other hand, the simulations of flow in the nozzle exhibit some sensitivity to the bubble spacing parameter in terms of the void fraction of the flow inside the nozzle. However, jet atomization, which is the breakup of the downstream flow, was always predicted for various spacing parameters.

6.3. Coherent mixing layer

The purpose of averaged equations for coherent layer of turbulent mixing is to eliminate most of the geometrical complexity through averaging. All fine scale geometrical details associated with complex interface positions are eliminated, and only large scale effects remain. Accordingly, applying stochastic models (Section 5.1) and the mixing edge evolution algorithm (Section 5.2) our two-dimensional study is initialized as a single sine wave perturbation to a planar mixing layer. In Fig. 4 we present results, plotting v_{1y} and v_{2y}, in their dependence on the space variables x, y. Note that the light fluid is on the top, and so v_{1y} is undefined in the (lower) region occupied exclusively by the heavy fluid while v_{2y} is undefined in the upper region. In the left frame, we display the initial conditions for v_{1y}. In the center frame, we show v_{1y} for a later time development of the instability. The influence of the macroscopic perturbation of the interface is evident. All v_{1y} velocities are negative, the blue being more strongly negative. Thus the light fluid is flowing most strongly into a dip on the lower edge of the mixing zone. The lower edge is the bubble edge. We interpret the macro disturbance as bubble and spike type structures on the bubble edge (and also the upper spike edge). In this terminology, the macro light fluid velocity is flowing into a macro bubble disturbance on the bubble edge of the mixing zone.

In the right frame of Fig. 4, we present the late time heavy fluid v_{2y} velocity. This velocity is everywhere positive, and is most strongly positive at the upper edge in the center. Using a similar terminology and analysis to that used for v_{1y}, we can say that the heavy fluid is flowing most strongly into a macro spike type disturbance of the spike (upper) edge of the mixing zone.

7. Conclusions

We have proposed using the front tracking method as a tool for the multiscale modeling and computation. The introducing of "intermediate scale" of the interfacial layer allows us to describe the interface dynamics accurately and to couple the microscale and the macroscale phenomena. The emphasis here is to use different continuum models to describe different scales. The interfacial physics are considered for a variety of problems, and the complex fluids are modeled in the multiscale setting. The proposed multiscale method allows us to deal with important physics at another flow scale. We see that this method makes accurate predictions for various test problems.

Acknowledgment

This work was supported in part by NNSA Grant DEFG5206NA26208, Army Research Office grant W911NF-0510413, and U.S. Department of Energy, Contract numbers DEAC0298CH10886.

References

Abgrall, R., Saurel, R., 2003. Discrete equations for physical and numerical compressible multiphase mixtures. Journal of Computational Physics 186, 361–396.

Alon, U., Hecht, J., Mukamel, D., Shvarts, D., 1994. Scale invariant mixing rates of hydrodynamically unstable interfaces. Physical Review Letters 72, 2867–2870.

Alty, T., Mackay, C.A., 1935. The accommodation coefficient and the evaporation coefficient of water. Proceedings of the Royal Society of London, Series A 149, 104–116.

Amsden, A.A., Ramshaw, J.D., O'Rourke, P.J., Dukowicz, J.K., 1989. KIVA: a computer program for two- and three-dimensional fluid flows with chemical reactions and fuel sprays. In: Computer Simulation for Fluid Flow Heat, and Mass Transport and Combustion for Recriprocating Engines.Hemisphere Publishing Corporation, New York, pp. 239–344.

Balibar, S., Caupin, F., 2003. Metastable liquids. Journal of Physics: Condensed Matter 15, s75–s82.

Banerjee, A., Andrews, M.J., 2006. Statistically steady measurements of Rayleigh–Taylor mixing in a gas channel. Physics of Fluids 18, 035107.

Berger M., 1987. Adaptive finite difference methods in fluid dynamics. von Karman Lecture Notes on CFD, NYU/DOE Report 03077-277.

Berger, M., Colella, P., 1989. Local adaptive mesh refinement for shock hydrodynamics. Journal of Computational Physics 82, 64–84.

Bergwerk, W., 1959. Proceedings of the Institution of Mechanical Engineers 173 (25), 655–660.

Brandt, A., 1977. Multi-level adaptive solutions to boundary-value problems. Mathematics of Computation 31, 333–390.

Brennen, C.E., 1995. Cavitation and Bubble Dynamics. Oxford University Press, New York.

Bukiet, B., 1988. Application of front tracking to two-dimensional curved detonation fronts. SIAM Journal on Scientific Computing 9, 80–99.

Bukiet, B., Gardner, C.L., Glimm, J., Grove, J.W., Jones, J., McBryan, O., Menikoff, R., Sharp, D.H., 1986. Applications of front tracking to combustion, surface instabilities and two-dimensional Riemann problems. In: Transactions of the Third Army Conference on Applied Mathematics and Computing, ARO Report No. 86-1, 1986, pp. 223–243.

Chen, Y., Glimm, J., Saltz, D., Sharp, D.H., Zhang, Q., 1996. A two-phase flow formulation for the Rayleigh–Taylor mixing zone and its renormalization group solution. In: Young, R., Glimm, J., Boston, B. (Eds.), Proceedings of the Fifth International Workshop on Compressible Turbulent Mixing. World Scientific, Singapore. ISBN 981-02-2910-0.

Cheng, B., Glimm, J., Saltz, D., Sharp, D.H., 1999. Boundary conditions for a two pressure two-phase flow model. Physica D 133, 84–105.

Cheng, B., Glimm, J., Sharp, D.H., 2000. Density dependence of Rayleigh–Taylor and Richtmyer–Meshkov mixing fronts. Physics Letters A 268, 366–374.

Chern, I.-L., Glimm, J., McBryan, O., Plohr, B., Yaniv, S., 1986. Front tracking for gas dynamics. Journal of Computational Physics 62, 83–110.

Colella, P., Woodward, P., 1984. The piecewise parabolic method PPM for gasdynamical simulation. Journal of Computational Physics 54, 174–201.

Dimonte, G., 2000. Spanwise homogeneous buoyancy-drag model for Rayleigh–Taylor mixing and experimental evaluation. Physics of Plasmas 7 (6), 2255–2269.

Drew, D.A., 1983. Mathematical modeling of two-phase flow. Annual Review of Fluid Mechanics 15, 261–291.

George, E., Glimm, J., 2005. Self-similarity of Rayleigh–Taylor mixing rates. Physics of Fluids 17, 054101-1–054101-13 Stony Brook University preprint number SUNYSB-AMS-04-05.

George, E., Glimm, J., Li, X.L., Marchese, A., Xu, Z.L., 2002. A comparison of experimental, theoretical, and numerical simulation Rayleigh–Taylor mixing rates. Proceedings of the National Academy of Sciences 99, 2587–2592.

Glimm, J., Sharp, D.H., 1997. Multiscale Science, SIAM News, October 1997.

Glimm, J., Marchesin, D., McBryan, O., 1980. Subgrid resolution of fluid discontinuities II. Journal of Computational Physics 37, 336–354.

Glimm, J., Saltz, D., Sharp, D.H., 1997. A general closure relation for incompressible mixing layers induced by interface instabilites. In: Jourdan, G., Houas, L. (Eds.), Proceedings of the Sixth International Workshop on the Physics of Compressible Turbulent Mixing. Imprimerie Caractère, Marseille, France, pp. 179–184.

Glimm, J., Saltz, D., Sharp, D.H., 1998a. Statistical evolution of chaotic fluid mixing. Physical Review Letters 80 (4), 712–715.

Glimm, J., Saltz, D., Sharp, D.H., 1998b. Two-pressure two-phase flow. In: Chen, G.-Q., Li, Y., Zhu, X. (Eds.), Nonlinear Partial Differential Equations. World Scientific, Singapore.

Glimm, J., Jin, H., Laforest, M., Tangerman, F., Zhang, Y., 2003a. A two pressure numerical model of two fluid mixtures. SIAM Journal on Multiscale Modeling and Simulation 1, 458.

Glimm, J., Li, X.-L., Liu, Y.-J., 2003b. Conservative front tracking with improved accuracy. SIAM Journal on Numerical Analysis 41, 1926–1947.

Glimm, J., Saltz, D., Sharp, D.H., 1999b. Two-phase modeling of a fluid mixing layer. Journal of Fluid Mechanics 378, 119–143.

Glimm, J., Grove, J.W., Li, X.-L., Zhao, N., 1999a. Simple front tracking. In: Chen, G.-Q., DiBebedetto, E. (Eds.), Contemporary Mathematics, vol. 238. American Mathematical Society, Providence, RI, pp. 133–149.

Hackbusch, W., 1985. Multi-Grid Methods and Applications. Springer, New York.

Hadjiconstantinous, N., 1999. Hybrid atomistic-continuum formulations and the moving contact-line problems. Journal of Computational Physics 154, 245–265.

Hansom, J.C.V., Rosen, P.A., Goldack, T.J., Fieldhouse, P., Oades, K., Cowperthwaite, N., Youngs, D.L., Mawhinney, N., Baxter, A.J., 1990. Radiation driven planar foil instability and mix experiments at the AWE HELEN laser. Laser and Particle Beams 8, 51–71.

Jin, H., Glimm, J., Sharp, D.H., 2006. Compressible two-pressure two-phase flow models. Physics Letters A 353, 469–474.

Jian, D., Brian, F., James, G., Xicheng, J., Xiaolin, L., Yunhua, L., Lingling, W., 2006. A simple package for front tracking. Journal of Computational Physics 213, 613–628 Stony Brook University preprint number SUNYSB-AMS-05-02.

Keyfitz, B., 1991. Change of type in simple models of two-phase flow. In: Shearer, M. (Ed.), Viscous Profiles and Numerical Approximation of Shock Waves. SIAM, Philadelphia, PA, pp. 84–104.

Landau, L., Lifshitz, E., 1980. Statistical Physics. Pregamon Press Ltd., Oxford, UK.

Lin, S.P., Reitz, R.D., 1998. Drop and spray formation from a liquid jet. Annual Review of Fluid Mechanics 30, 85–105.

Liu, X.F., George, E., Bo, W., Glimm, J., 2006. Turbulent mixing with physical mass diffusion. Physical Review E 73, 056301-1–056301-8.

Liu, X.F., Li, Y.H., Glimm, J., Li, X.L., 2007. A front tracking algorithm for limited mass diffusion. Journal of Computational Physics 222 (2), 644–653.

Lu, T., Samulyak, R., Glimm. J., 2005. Direct numerical simulation of bubbly flows and its applications. Physics of Fluid Engineering, submitted for publication.

Oron, D., Arazi, L., Kartoon, D., Rikanati, A., Alon, U., Shvarts, D., 2001. Dimensionality dependence of the Rayleigh–Taylor and Richtmyer–Meshkov instability late-time scaling laws. Physics of Plasmas 8, 2883–2889.

Ransom, V.H., Hicks, D.L., 1984. Hyperbolic two-pressure models for two-phase flow. Journal of Computational Physics 53, 124–151.

Reitz, R.D., Bracco, F.V., 1982. Mechanism of atomization of a liquid jet. Physics of Fluids 25, 1730–1742.

Reitz, R.D., Bracco, F.V., 1986. Mechanisms of breakup of round liquid jets. The Encyclopedia of Fluid Mechanics. Gulf Pub. Co., Book Division.

Weinan, E., Bjorn, E., 2003. The heterogeneous multiscale methods. Communications in Mathematical Sciences 1, 87–132.

Weiqing, R., Weinan, E., 2005. Heterogeneous multiscale method for the modeling of complex fluids and micro-fluidics. Journal of Computational Physics 204, 1–26.

Scannapieco, A., Cheng, B., 2002. A multifluid interpenetration mix model. Physics Letters A 299, 49–64.

Schmidt, D.P., Rutland, C.J., Corradini, M.L., 1999. Cavitation in two-dimensional asymmetric nozzles. SAE 1999-01-0518, February 1999. SAE International Congress.

Sharp, D.H., 1984. An overview of Rayleigh–Taylor instability. Physica D 12, 3–18.

Smeeton, V.S., Youngs, D.L., 1987. Experimental investigation of turbulent mixing by Rayleigh–Taylor instability (part 3). AWE Report Number 0 35/87, 1987.

Stewart, H.B., Wendroff, B., 1984. Two-phase flow: models and methods. Journal of Computational Physics 56, 363–409.

Van Carey, P., 1992. Liquid-vapor phase-change Phenomena. Hemisphere Publishing Corporation, New York, NY.

Van Leer, B., 1979. Towards the ultimate conservative difference scheme: V. A second order sequel to Godunov's method. Journal of Computational Physics 32, 101–136.

Ventikos, Y., Tzabiras, G., 2000. A numerical method for the simulation of steady and unsteady cavitating flows. Computers and Fluids 29, 63–88.

Wallis, G., 1969. One-dimensional Two-phase Flow. McGraw-Hill, New York.

Wilson, K., 1975. The renormalization group: critical phenomena and the kondo problem. Reviews of Modern Physics 47, 773–840.

Xu, Z.L., Lu, T., Samulyak, R., Glimm, J., Ji, X.M., 2006a. Dynamic phase boundaries for compressible fluids. SIAM Journal on Scientific Computing, submitted for publication.

Xu, Z.L., Kim, M., Oh, W., Glimm, J., Samulyak, R., Li, X.L., Tzanos, C., Lu, T., 2006b. Discrete bubble modeling of unsteady cavitating flow. International Journal for Multiscale Computational Engineering 4, (5–6).